applied optics

Extended overlap function computation method for atmospheric lidars

MATTEO FACCIONI,[1,2,*] ANDREAS MEZGER,[1] AND PATRICK VRANCKEN[1]

[1] Deutsches Zentrum für Luft- und Raumfahrt (DLR), Institut für Physik der Atmosphäre, Oberpfaffenhofen, Germany
[2] Technical University of Munich, School of Engineering and Design, Department of Aerospace and Geodesy, Institute of Astronomical and Physical Geodesy, Munich, Germany
*matteo.faccioni@dlr.de

Received 4 May 2026; revised 15 June 2026; accepted 30 June 2026; posted 1 July 2026; published 23 July 2026

In this publication, an extended method for calculating the overlap function for atmospheric lidars is introduced. A generic procedure is proposed to compute the overlap function, also referred to as geometrical function, geometric compression, or geometrical form factor. This procedure implements both ray-tracing and physical optics propagation methods to simulate the propagation of the transmitted beam in the atmosphere, and its back-propagation to the receiver telescope, allowing to take into account different factors such as the profile of the transmitted beam, the turbulent atmosphere, the lidar receive system's optical aberrations, and different lidar configurations. Even though the scope of the publication is for introducing the method without analyzing in detail the dependencies of the overlap function on one of these factors, three applications of the method are described: quantifying the impact on the overlap function of the circular obstruction in a mono-axial lidar, simulating the effects of different focus positions on the lidar signal, and computing the overlap function considering a flat-top transmitted beam.

https://doi.org/10.1364/AO.604477

1. INTRODUCTION

Quantifying the amount of signal collected by the detector with respect to the total backscattered signal in the lidar full field of view (FFOV), the overlap function is a key parameter in atmospheric lidar design. Given the wide variety of atmospheric lidars, from the ones working at close range [1] to the ones working at the last layers of the Earth atmosphere [2], the overlap function depends on a large number of parameters. For example, in the case of a close-range lidar, this function takes into account the fact that a generic lidar system images an object (i.e., the atmospheric backscatter) placed at different distances while keeping the detector and the imaging optics at a fixed distance, causing the object to be perfectly focused only at one specific distance. At all other distances, the detector sees a more or less blurred image of the backscatter, up to the extreme case in which the backscatter image is far greater than the detector area, resulting in a reduced signal collected by the detector. Hence, it is fundamental to optimize the lidar design, trying to keep these losses at a minimum for the desired ranges of interest. In general, the factors influencing the overlap function are the transmitted beam parameters (e.g., beam divergence), parameters related to the configuration of the lidar system (e.g., central obscuration due to the receiver telescope configuration), or effects that influence the beam propagation in the atmosphere (e.g., turbulence), or in the optical system (e.g., aberrations). Given the importance of the overlap function in the design of lidar systems, different methods for computing it have been proposed over the years. These can be subdivided into ray-tracing (RT) [3,4], analytical solutions [5–8], experimental methods [9–14], or a combination of RT and Fourier optics (FO) propagation methods [15]. RT methods usually rely on commercial software and are a good solution when it is needed to design the optical components of the system [16]. However, they are usually black boxes for which it is difficult to achieve a flexible simulation (e.g., simulating different beam profiles). Analytical solutions allow to describe the overlap function with a single equation; however, their limitation stands in the number of assumptions that are needed, such as approximating geometrical optics equations [17], not considering optical aberrations [18], or considering an ideal TEM_{00} beam profile [19]. Finally, experimental methods are the ideal choice during measurement campaigns; however, they cannot be used for modeling the overlap function of a lidar system during the design process.

All the presented methods focused on the dependence of the overlap function on the transmitted beam parameters and receiver telescope layout. However, the authors have found no method that considers the turbulent atmosphere effects on the overlap function computation. One of the effects of a turbulent atmosphere on a propagating optical beam is the phenomenon defined as *beam wander* [20], causing the transmitted beam centroid to be displaced from its nominal position. Atmospheric lidars have a small FFOV, and this effect could drift the transmitted beam to the edge of the receiver telescope FFOV [21], affecting the overlap function. The modeling and quantification of the effects of a turbulent atmosphere on the overlap function are not the purpose of this publication, and these will be addressed in a subsequent work. Nevertheless, the present publication describes in detail the set of equations and the procedure that will be used for this analysis.

Another topic, where a precise overlap function computation would be of interest, is the possible optimization of a lidar system considering different transmitted beam profiles. Due to the rapid development of new forms of light shaping [22], it is interesting to quantify the possible advantages of new lidar systems using different beam profiles than the idealized Gaussian laser mode TEM_{00}. A first investigation in this regard was carried out around 20 years ago, considering the performance of a lidar implementing a transmitted annular beam profile [23,24]. However, no other studies on this topic have been found in the atmospheric lidar community.

Finally, the need for a highly accurate overlap function model is of great importance for self-aligning lidar systems based on the overlap function as a cost function. Over the years, a wide variety of alignment systems and procedures have been proposed and developed, depending on the lidar's configuration. It is possible to distinguish between alignment systems used for continuous beam stabilization [25] and those used for a single alignment, varying the direction of the transmitted beam [26–28], or acting on both the transmitter and receiver axes [29]. All the methods belonging to the latter family share the same algorithm architecture, aligning the instrument through the data measured by means of a mapping procedure. At the Deutsches Zentrum für Luft- und Raumfahrt, it is being investigated whether merging the measured lidar signal and an accurate overlap function model could lead to a faster alignment procedure.

The objective of this publication is to propose a method that addresses these open topics, presenting a set of equations and a procedure that the reader can use to compute the overlap function by implementing the equations provided in Appendices B and C in an open-source programming language, such as python [30].

This publication is structured as follows: in the first section, a brief introduction to optical propagation methods is provided. The proposed method is presented in the second section, while some of its applications are described in the third section.

2. BRIEF INTRODUCTION TO OPTICAL PROPAGATION METHODS

In this section, a short overview of different optical propagation methods is given. In general, it is possible to distinguish between two main approaches while propagating an optical beam in a system:

- RT: this approach is used when the wave nature of light can be ignored, ensuring a fast simulation at any desired resolution;
- physical optics: this approach is used whenever it is needed to investigate the wave nature of light (e.g., coherent effects) [31], or when there are no analytical solutions describing the propagation of the transmitted beam (e.g., a flat-top beam).

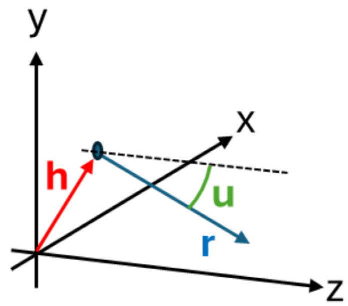

Fig. 1. Single ray representation. Light blue indicates the ray; black, the reference system; red, the height of the ray; and green, the angle of the ray.

Both approaches are described in more detail in the next subsections.

A. RT Propagation

RT propagation methods describe an optical beam using a finite number of rays propagating along the direction normal to the beam wavefront. All these rays obey Fermat's principle of least time, choosing the path that minimizes the time taken, and each of them is characterized by a certain flux, usually expressed in W, a vector height $\mathbf{h} = (h_x, h_y, h_z)$, and a vector angle $\mathbf{u} = (u_x, u_y, u_z)$, describing the ray's angles with respect to the system optical axis. A ray $\mathbf{r}$ defined in this way is shown in Fig. 1. In general, it is more convenient to describe the ray using its optical direction cosine, defined as $v = n \sin u$, where n is the index of refraction of the medium in which the ray is propagating. However, in the proposed method, assuming the paraxial approximation to hold, the angle $\mathbf{u}$ is used. Indeed, in a generic atmospheric lidar, the FFOV is always very small, and the paraxial assumption can be considered always valid. The RT propagation method used in this publication is the well-known paraxial ABCD matrices method [32]. This technique is preferred to the more exact complex ABCD matrices method [33,34], assuming the beam to be propagated to the far field. In the case an even more accurate simulation is needed (e.g., taking into consideration freeform optical components), the differential RT method should be used [35].

B. Physical Optics Propagation

Three of the most used physical optics propagation methods are based on:

- **Finite difference time domain (FDTD)**: following the work in [36], this approach solves the propagation of an electromagnetic wave by replacing Maxwell's equations with a set of finite difference equations.
- **Gaussian beam decomposition (GBD)**: following the work in [37], this approach decomposes a beam into Gaussian beamlets and propagates them until the surface of interest using complex RT. On this surface, the resulting wave is computed by superimposing all the beamlets, taking into consideration their amplitude and phase.

- **FO**: this approach solves the beam's propagation by decomposing the optical wave using Fourier analysis. Each Fourier component represents a plane wave propagating in a certain direction, and the propagated beam on the surface of interest is computed by adding the contributions of these plane waves' amplitudes and phases [38].

In this publication, the latter class of methods is implemented. The main reference for developing FO propagation methods is the comprehensive work in [39]. Following the FO method, the propagating beam is represented by the scalar perturbation $\mathcal{U} = A\mathrm{e}^{-\mathrm{i}k\Phi}$, where $A(x, y)$ is the beam amplitude, $\Phi(x, y)$ is the beam phase, and $k = 2\pi/\lambda$, where λ is the beam wavelength. By means of the Fourier transform, it is possible to decompose the perturbation $\mathcal{U}$ into elementary inputs, and considering the system as linear, its response to each of these elementary inputs can be superimposed to obtain the final total response of the system. The propagation of the perturbation $\mathcal{U}$ can be computed by means of the Huygens–Fresnel principle [40], considering the disturbance at the previous instant z_0 to be composed of spherical disturbance emitters that sum up coherently at the point P. Mathematically, the Huygens–Fresnel principle can be expressed using the Rayleigh–Sommerfeld diffraction formula [41]:

$$\mathcal{U}(x, y) = \frac{z}{\mathrm{i}\lambda} \iint_S \mathcal{U}(\epsilon, \eta) \frac{\mathrm{e}^{\mathrm{i}kr_{mp}}}{r_{mp}^2} \mathrm{d}\epsilon \mathrm{d}\eta, \tag{1}$$

where $\mathcal{U}(\epsilon, \eta)$ is the perturbation of the mth source located at the point (ϵ, η, z_0), on the surface S, z is the propagation distance, ϵ and η are the coordinates of the plane, where the input perturbation is computed, and the term $\mathrm{e}^{\mathrm{i}kr_{mp}}/r_{mp}$ represents a diverging spherical wave, where r_{mp} is the distance between the mth source and the point $P(x, y, z)$, expressed as

$$r_{mp} = \sqrt{(z - z_0)^2 + (x - \epsilon)^2 + (y - \eta)^2}. \tag{2}$$

In Appendix A, it is explained how Eq. (1) can be solved for different propagation distances.

3. EXTENDED OVERLAP FUNCTION METHOD OVERVIEW

Before describing the proposed method in detail, it is convenient to define some terms that are used frequently throughout this publication:

- the plane from where the beam is transmitted into the atmosphere is defined as the *transmitting plane* (TP). This corresponds to a range distance $z = 0$ m;
- the plane from where the beam is backscattered to the receiver telescope is defined as the *scattering plane* (SP). The ith scattering plane, SP_{z_i}, is placed at range z_i;
- the whole receiver telescope is modeled by a single plane, defined by the receiver aperture stop (AS) [42];
- the plane, where the overlap function is computed is defined as the *detector plane* (DP). According to the kind of detector, different filters can be defined (e.g., if a fiber is used, its numerical aperture (NA) would limit the received beam's accepted angles).

The method can then be described by the following steps:

1. **Modeling the transmitted beam**: the transmitted beam irradiance, E_{TP}, in $\mathrm{W\,m^{-2}}$, is computed at the TP. At this step, possible errors induced by the optical elements in the transmitted channel (e.g., misalignment) can be introduced;
2. **Propagating the beam in the atmosphere**: the transmitted beam is then propagated through the atmosphere to the ith SP_{z_i}, at the distance z_i, where the beam irradiance E_{z_i} is computed. This can be done using the ABCD method [32], if analytical solutions describing the beam propagation are known (e.g., for a TEM_{00} beam [43]), or using FO. In the former case, the effects of a turbulent atmosphere are modeled using analytical solutions [20], while in the latter case, the phase screen method [44] is used;
3. **Computing the volume backscattered intensity**: the volume backscattered intensity of the ith SP_{z_i}, in $\mathrm{W\,sr^{-1}\,m^{-3}}$, is computed by multiplying the transmitted beam irradiance by the volume backscattering coefficient, β, in $\mathrm{m^{-1}\,sr^{-1}}$
$$I_{z_i} = E_{z_i}\beta, \tag{3}$$
where the value for β can be retrieved from the literature [45,46], or in the case of bi-static systems, it can be computed from theoretical aerosol size distributions [47], using the Mie solution for an electromagnetic wave scattered by spherical particles [48]. This can be done using different software, such as the *miepython* package [49], the BHMIE algorithm [50], or, in the case of non-spherical particles, MOPSMAP [51];
4. **Propagating the backscattered wave to the receiver aperture stop**: in the next steps, the backscattered wave is modeled as the incoherent sum of point-source emitters placed on the ith SP_{z_i} [52], not considering any coherent phenomena [53]. However, it would be possible to consider the backscattering coherent enhancement using analytical solutions [54] or by propagating the whole backscattered wave using FO. The total beam irradiance at the receiver aperture stop, E_{AS}, is computed as [55]
$$E_{\mathrm{AS}} = I_{z_i}\Omega_{z_i}\delta_z, \tag{4}$$
where Ω_{z_i} is the solid angle subtended by the AS, and δ_z is the depth of the considered scattering volume. As in the second step, the irradiance spatial distribution can be computed using RT or FO propagation methods. Within the proposed method, it is always possible to select the kind of propagation for the transmitted and backscattered wave, thus it could be thought as a generalization of the method proposed by Berezhnyy [15];
5. **Propagating the backscattered wave to the detector plane**: in this step, the optical aberrations of the receiving channel are modeled. This is done using Seidel coefficients [56], in the case of RT propagation, or using Zernike polynomials [57], in the case of FO propagation. The aberrated beam is then propagated to the DP;
6. **Computing the overlap function**: finally, the overlap function is computed as the intersection between the detector surface and the filtered beam irradiance on the DP

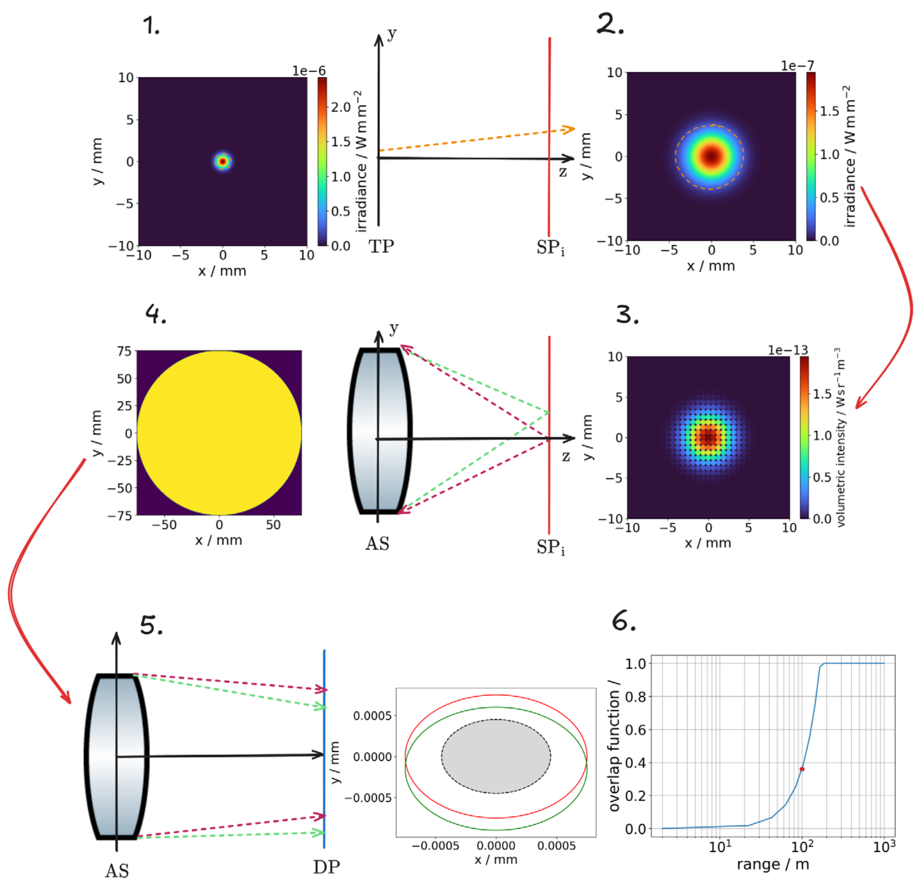

Fig. 2. Proposed method's steps. In step (1), the transmitted beam is modeled. The orange dashed line represents the beam's waist. In step (2), the propagation of the transmitted beam to the scattering plane SP_{100}, at range $z = 100$ m, is shown. The increased beam's size is represented by a dashed orange line. In step (3), the volume backscattered intensity is computed, assuming $\beta = 10^{-6}$ m^{-1} sr^{-1}. In step (4), the backscattered wave is propagated to the receiver telescope AS. In the figure, the back-propagation of only two emitters is shown with red and green dashed lines, and an aberration-free system is considered. In step (5), the beam is propagated to the detector plane. The image sizes of the two emitters are shown with a red and a green circle, respectively. In step (6), the overlap function is computed. The red dot represents the overlap function value computed at range $z = 100$ m and the blue line represents the overlap function.

using the circle intersection equation [5]. For example, if the detector is a fiber with a specific NA_f, the filter would accept only the part of the beam with $NA \leq NA_f$.

Considering a transmitted TEM_{00} ideal beam, the method's steps are graphically shown in Fig. 2. The equations used in the case of RT and FO propagation methods are described in detail in Appendices B and C, respectively.

4. APPLYING THE EXTENDED OVERLAP COMPUTATION METHOD

In this section, three different applications of the method are presented:

- computing the effect of the receiver telescope's central obstruction on the overlap function;
- computing the effect of moving the fiber position on the overlap function;
- computing the overlap function for a flat-top beam.

All the examples presented in this section consider a mono-axial lidar system with the parameters listed in Table 1. In this case, the NA of the fiber is considered to be larger than the telescope FFOV; hence, the fiber and the detector are considered as equivalent.

A. Effect of the Receiver Telescope's Central Obstruction

In this example, the effect of the central circular obstruction, which is inherent in the use of a Newtonian or Cassegrain telescope [5,7,19,52], on the overlap function of the mono-axial lidar shown in Fig. 3 is quantified. As a lidar is not an imaging system, in this example, the RT propagation method is used,

Table 1. Parameters of the Lidar System Considered in the Applications Presented in Section 4

Parameter	Value
Receiver focal length	1 m
Receiver diameter	150 mm
Full field of view (FFOV)	0.9 mrad
Ranges considered	5 m–1000 m
Beam waist	1 mm

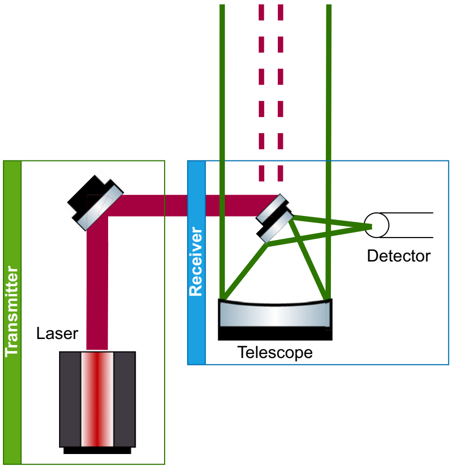

Fig. 3. Mono-axial lidar system considered in the example. Red lines represent the transmitted beam, while the green lines represent the received backscattered wave.

and an axis-symmetric TEM_{00} transmitted beam is assumed. In the considered lidar configuration, it is clear that the central obstruction affects only the received backscattered signal, therefore, the simulation of the transmitted beam remains unchanged compared with that described in Appendix B. On the other hand, the circular obstruction blocks part of the backscattered wave, causing a reduction in the collected signal at the detector. To simulate this effect, four rays are traced from the SP. These rays are used to compute, in order:

1. the reduction of the backscattered wave flux due to the central obstruction blockage;
2. the circles of confusion on the DP of the shadow region, generated by the central obstruction and of the backscattered wave, respectively.

The ray tracing of the four rays for a single emitter, and the results obtained considering a central obstruction with radius 0, 20, and 40 mm, respectively, and a distance between the receiver telescope and the central obstruction of $z_{\text{obs}} = 700$ mm, are shown in Fig. 4. It is clear how the central obstruction decreases the received signal, both by increasing the range at which the first signal is collected and by decreasing the peak of the overlap function.

B. Effect of Moving the Fiber Position

In this example, the overlap function of a mono-axial lidar assuming different defocus distances $\delta_{f_1} = 0$ mm, $\delta_{f_2} = 2$ mm, $\delta_{f_3} = 5$ mm, and $\delta_{f_4} = 8$ mm, is evaluated. The quantity δ_f corresponds to the displacement of the fiber behind the effective focal length of the receiver telescope. The obtained overlap functions are shown in Fig. 5. By moving the fiber position, it is possible to have a full overlap at shorter ranges, having a higher lidar signal at the desired range. The reason is that the receiver telescope is no longer optimized for an object placed at infinity, and the new optimized object distance can be roughly quantified as

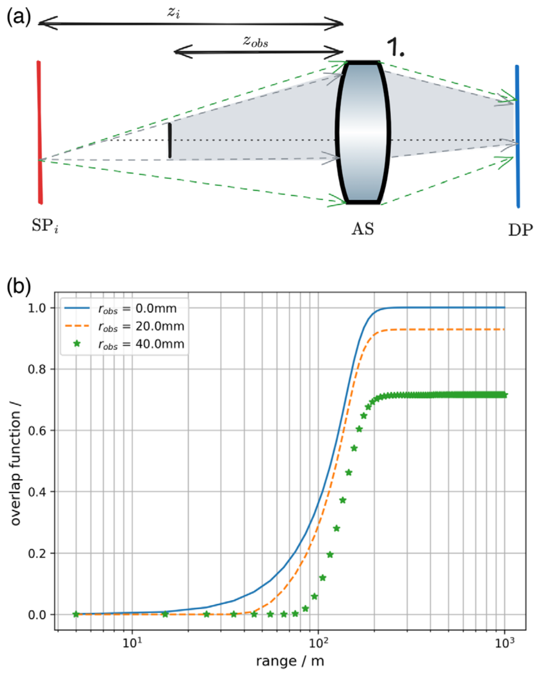

Fig. 4. (a) Steps followed to simulate the effect of the central obstruction: the red line indicates the SP$_i$ from where an emitter is propagated first to the receiver AS, where the reduction of flux is computed, then to the DP, where the circles of confusion of the shadowed region and of the signal are computed. The dashed green line indicates the two rays representing the backscattered wave and dashed gray line indicates the rays representing the blocked region. The gray area represents the shadowed area caused by the central obstruction. (b) The overlap functions computed considering a circular central obstruction: the blue line indicates the result obtained assuming $r_{\text{obs}} = 0$ mm, dashed orange, the result assuming $r_{\text{obs}} = 20$ mm, and green stars, the result assuming $r_{\text{obs}} = 40$ mm.

$$z_{\text{opt}} = \frac{f(f + \delta_f)}{\delta_f}, \tag{5}$$

where f is the receiver effective focal length. In the case of lidars measuring at close distances [1,58], this solution can be implemented to enhance the lidar signal at the desired range. Moreover, this feature is useful also for very long range lidars, such as HELIX [59]. HELIX is a ground-based, fluorescence lidar developed to study Helium over the ranges between 300 and 800 km, from the thermosphere to the exosphere. Due to the low return signal, it takes several minutes of averaged exposures to achieve a significant signal-to-noise ratio (SNR). This makes it impractical to focus the receiving telescope onto a layer at the distance of interest. In this case, to optimize the overlap between the transmitted laser beam and the receiver telescope FFOV two steps are required:

1. the telescope is focused at an atmospheric layer at 18.5 km altitude, where there is enough signal caused by Rayleigh scattering of the laser. This is done by shifting the fiber until the maximum return signal is found;
2. then, the fiber is shifted by a fixed offset to achieve the best overlap in the mesosphere. The required offset has been determined by optimizing the overlap function, computed using RT propagation.

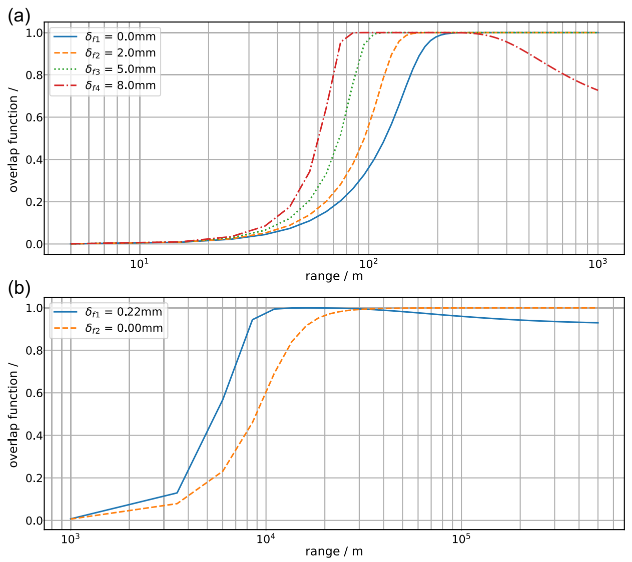

Fig. 5. (a) Overlap functions for different defocus distances: the blue line indicates a defocus distance $\delta_{f_1} = 0.0$ mm; orange dashed line, a defocus distance $\delta_{f_2} = 2$ mm; green dotted line, a defocus distance $\delta_{f_3} = 5$ mm; and red dashed-dotted line, a defocus distance $\delta_{f_4} = 8$ mm. (b) HELIX overlap functions for different defocus distances: the blue line indicates a defocus distance $\delta_{f_1} = 0.22$ mm and orange dashed line, a defocus distance $\delta_{f_2} = 0.00$ mm.

The obtained overlap functions considering a FFOV of 61 μrad, a receiver telescope diameter of 762 mm, a focal length of 1875 mm, a beam waist $w_0 = 7.2$ mm, and the two different defocus distances $\delta_{f_1} = 0.22$ mm and $\delta_{f_2} = 0.00$ mm, are shown in Fig. 5.

C. Overlap Function of a Flat-Top Beam

In this example, a flat-top beam (i.e., with a uniform irradiance profile) is propagated considering an aberration-free system. In general, a flat-top beam does not have a constant irradiance all along its path, but this is achieved at a certain design distance. In this example, it is considered to design the beam in such a way as to be flat-top in the far field of the aperture. This is achieved by using a diffuser optical element [22], designed using the Gerchberg–Saxton (GS) algorithm [60]. Assuming a beam waist $w_0 = 1$ mm, and a desired flat-top angular diameter of $\Psi = 0.36$ mrad in the far field, the obtained beam irradiance for four different ranges is shown in Fig. 6. Moreover, the overlap function considering the same lidar system parameters and an ideal TEM_{00} transmitted beam has been computed using both RT and FO propagation methods, and the percentage of their relative difference is computed as

$$\varepsilon_G = 100\% \times \left| 1 - \frac{G_{\mathrm{RT}}}{G_{\mathrm{FO}}} \right|, \tag{6}$$

where G_{RT} and G_{FO} are the overlap functions computed using RT and FO propagation methods, respectively. The obtained overlap functions are shown in Fig. 7. In this simple application, the comparison leads, quite logically, to the conclusion that for a smaller beam angular diameter, the full overlap is reached at a shorter range. However, this simple example is intended to demonstrate the potential of the proposed method

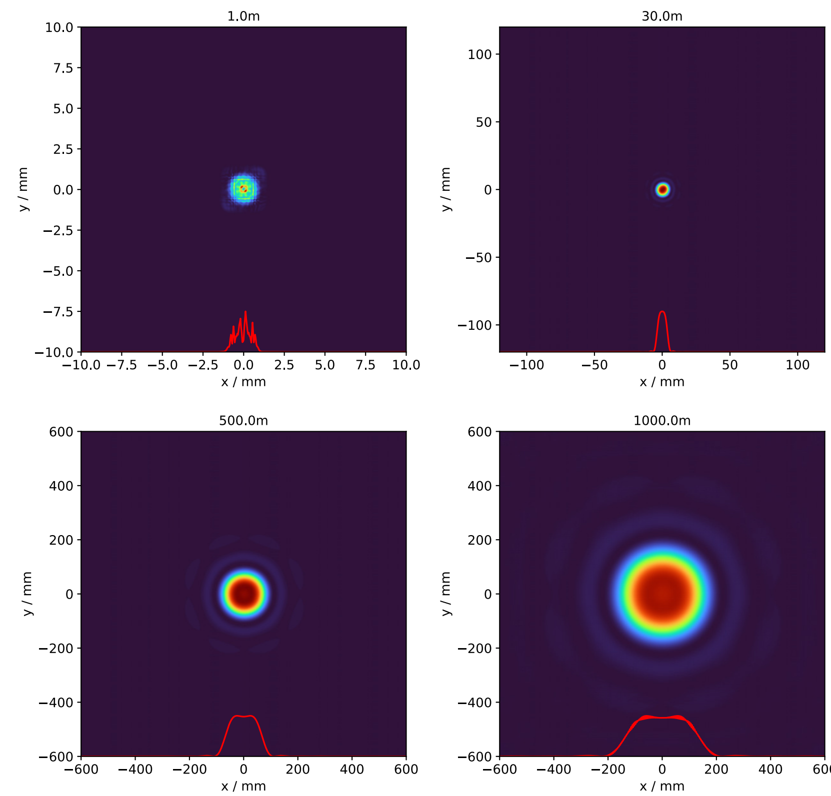

Fig. 6. Flat-top beam propagation for different ranges. In each figure, the beam irradiance at the range specified on top of each figure is represented.

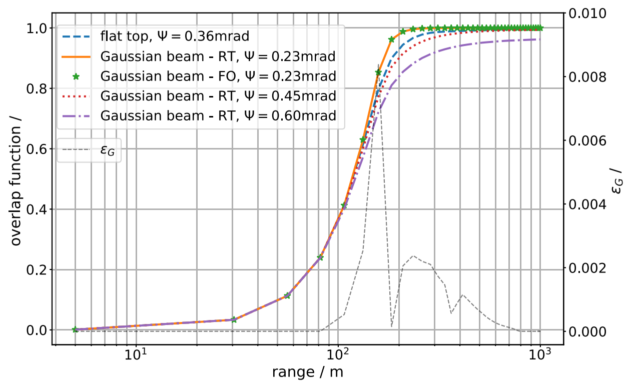

Fig. 7. Overlap functions computed for different beam shapes and divergence angles. The dashed blue line indicates the overlap function of a flat-top beam with a 0.36 mrad angular diameter; orange line, the overlap function of a Gaussian beam with a 0.23 mrad angular diameter computed using RT; green stars, the overlap function of a Gaussian beam with a 0.23 mrad angular diameter computed using FO; dotted red line, the overlap function of a Gaussian beam with a 0.45 mrad angular diameter computed using RT; dashed-dotted purple line, the overlap function of a Gaussian beam with a 0.60 mrad angular diameter computed using RT; and black dashed line, the percentage of the relative difference between the overlap function of an ideal TEM_{00} beam computed using RT and FO propagation methods.

in quantifying the overlap function for different kinds of beam profiles, allowing to test whether new beam profiles could lead to an improved overlap function for atmospheric lidar systems. Moreover, the comparison between the overlap functions computed using RT and FO propagation methods shows a very small error, ensuring that the two methods are equivalent in the case of a transmitted TEM_{00} beam. More details regarding the comparison between RT and FO propagation methods are given in Appendix D.

5. CONCLUSION

This publication presented an extended method for computing the overlap function of atmospheric lidars that allows one to consider various factors that are not normally taken into account, such as the turbulent atmosphere or the system optical aberrations. A system analysis of these effects will be presented in a subsequent publication. The proposed method allows to simulate the propagation of the optical beam using two types of propagation: RT or FO. The latter, modeling the propagation of the optical wave in a generalized way, allows to simulate a wide variety of beams, from the simplest TEM_{00} to the most complex shapes (e.g., vortex beams or even structured light). For both kinds of propagation methods, the theoretical foundations and their implementation have been presented. In the three described applications, it has been shown how the proposed method can be used to simulate different parameters influencing the overlap function, and consequently the performance of a lidar system. Finally, the presented method is being integrated into AMALIA, a lidar digital twin being developed at the Deutsches Zentrum für Luft- und Raumfahrt, and it is being tested alongside an automatic alignment lidar algorithm.

APPENDIX A: FO PROPAGATION REGIONS

The Rayleigh–Sommerfeld diffraction equation, as described in Eq. (1), can be simplified depending on the propagating distance, obtaining three different propagation regions:

- **Angular spectrum (AnS) region**: in this case, the beam is propagated to a surface close to the source, and no further simplifications can be done. The propagation of the perturbation $\mathcal{U}$ to the point P using FO can be written as

$$\mathcal{U}(x, y) = \iint_{-\infty}^{+\infty} \Upsilon\left(f_\epsilon, f_\eta\right) e^{ik\sqrt{1-f_\epsilon^2\lambda^2-f_\eta^2\lambda^2}z} \times \operatorname{circ}\left(\lambda\sqrt{f_\epsilon^2+f_\eta^2}\right) e^{\left[i2\pi\left(f_\epsilon x+f_\eta y\right)\right]} d f_\epsilon d f_\eta, \tag{A1}$$

where $\Upsilon(f_\epsilon, f_\eta)$ is the Fourier transform of $\mathcal{U}(\epsilon, \eta)$, f_x and f_y are the spatial frequencies along the x-axis and y-axis, respectively, and the circ function is defined as

$$\operatorname{circ}(r) = \begin{cases} 1 & r \le 1 \\ 0 & r > 1 \end{cases}. \tag{A2}$$

Eq. (A1) can be expressed in a simplified way using the notation suggested in [61].

- **Fresnel (FRE) region**: this case is valid when the beam is propagated to the near field of the aperture, with the propagating distance being

$$z^3 \gg \frac{\pi}{4\lambda} \max\left\{\left[(x-\epsilon)^2 + (y-\eta)^2\right]^2\right\}. \tag{A3}$$

Then, the distance r_{mp} can be expressed as

$$r_{mp} \approx z\left[1 + \frac{1}{2}\left(\frac{x-\epsilon}{z}\right)^2 + \frac{1}{2}\left(\frac{y-\eta}{z}\right)^2\right]. \tag{A4}$$

Substituting Eq. (A4) in Eq. (1), the Fresnel diffraction integral is obtained

$$\mathcal{U}(x, y) = \frac{e^{ikz}}{i\lambda z} e^{i\frac{k}{2z}\left(x^2+y^2\right)} \iint_{-\infty}^{+\infty} \mathcal{U}(\epsilon, \eta) e^{i\frac{k}{2z}\left(\epsilon^2+\eta^2\right)} e^{-i\frac{k}{z}(x\epsilon+y\eta)} d\epsilon d\eta. \tag{A5}$$

- **Fraunhofer (FRA) region**: in this case, the beam is propagated to the far field of the aperture, and the distance shall be

$$z \gg \frac{k\max\left(\epsilon^2+\eta^2\right)}{2}. \tag{A6}$$

Eq. (1) can then be written as

$$\mathcal{U}(x, y) = \frac{e^{ikz} e^{i\frac{k}{2z}\left(x^2+y^2\right)}}{i\lambda z} \iint_{-\infty}^{+\infty} \mathcal{U}(\epsilon, \eta) e^{\left[-i\frac{k}{z}(x\epsilon+y\eta)\right]} d\epsilon d\eta, \tag{A7}$$

where, apart from the constant multiplicative factors preceding the integral, it is possible to recognize that the perturbation at the point P is expressed as the Fourier transform of the perturbation at the source $\mathcal{U}(\epsilon, \eta)$.

APPENDIX B: COMPUTING THE OVERLAP FUNCTION USING THE PARAXIAL ABCD MATRICES

Considering an aberration-free system, a transmitted TEM_{00} beam with a waist radius at the TP equal to w_0 and a divergence angle equal to θ, and considering only the two components along the x and y axes of the height and angle vectors $\mathbf{h}$ and $\mathbf{u}$, the ABCD matrices method implementation for the different steps presented in Section 3 is the following:

1. **Modeling the transmitted beam**: the centroid ray $\widetilde{\mathbf{r}_0}$ and the marginal ray $\widehat{\mathbf{r}_0}$ are defined as

$$\widetilde{\mathbf{r}_0} = \begin{pmatrix} \widetilde{\mathbf{h}_0} \\ \widetilde{\mathbf{u}_0} \end{pmatrix}, \tag{B1}$$

$$\widehat{\mathbf{r}_0} = \begin{pmatrix} \widehat{\mathbf{h}_0} \\ \widehat{\mathbf{u}_0} \end{pmatrix}, \tag{B2}$$

where the beam's centroid position is $\widetilde{\mathbf{h}_0} = (\widetilde{h_{x,0}} = 0\ \mathrm{mm}, \widetilde{h_{y,0}} = 0\ \mathrm{mm})$, the beam's marginal position is $\widehat{\mathbf{h}_0} = (\widetilde{h_{x,0}}, \widetilde{h_{y,0}} + w_0)$, and $\widetilde{\mathbf{u}_0}$ and $\widehat{\mathbf{u}_0}$ represent the centroid and marginal ray angles at the TP, respectively, being

$$\widetilde{\mathbf{u}_0} = \left(\delta_{u_{y,0}} = 0\ \mathrm{rad}, \delta_{u_{y,0}} = 0\ \mathrm{rad}\right), \tag{B3}$$

$$\widehat{\mathbf{u}_0} = \left(\delta_{u_{y,0}}, \delta_{u_{y,0}} + \theta\right), \tag{B4}$$

where $\delta_{u_{i,0}}$ is the transmitted beam misalignment of the ith axis with respect to the receiver telescope optical axis.

2. **Propagating the beam in the atmosphere**: the centroid and marginal rays are propagated to the range z, on the SP_z, as

$$\mathbf{r}_z = \mathbf{M}_{\mathrm{FS}}(z)\mathbf{r}_0, \tag{B5}$$

where $\mathbf{M}_{\mathrm{FS}}$ is the matrix representing the free-space propagation for a distance z

$$\mathbf{M}_{\mathrm{FS}}(z) = \begin{bmatrix} 1 & z \\ 0 & 1 \end{bmatrix}. \tag{B6}$$

3. **Computing the volume backscattered intensity**: the incident irradiance of the transmitted beam at the SP_z is computed as a Gaussian profile, with a beam radius equal to $w_z = \sqrt{\widehat{h_{x,z}}^2 + \widehat{h_{y,z}}^2}$, on the grid $\mathbf{E}_z$, centered on the centroid ray position $\widetilde{\mathbf{h}_z} = (\widetilde{h_{x,z}}, \widetilde{h_{y,z}})$, with spatial dimension $\mathbf{d} = (d_x, d_y)$, and composed of $n_x \times n_y$ emitters. The position of each ijth emitter is computed as

$$h_{x,z,ij}\left(i, \widetilde{h_{x,z}}\right) = \left(i - \frac{n_x}{2}\right)\frac{d_x}{n_x} - \widetilde{h_{x,z}}, \tag{B7}$$

$$h_{y,z,ij}\left(j, \widetilde{h_{y,z}}\right) = \left(j - \frac{n_y}{2}\right)\frac{d_y}{n_y} - \widetilde{h_{y,z}}, \tag{B8}$$

where i and j are the row and column indices of the grid $\mathbf{E}_z$, respectively. As shown in Eq. (3), the volume intensity grid $\mathbf{I}_z$ is obtained by multiplying $\mathbf{E}_z$ by the volume backscattering coefficient β.

4. **Propagating the backscattered wave to the receiver aperture stop**: the propagation of each emitter to the AS is computed using two rays. Considering the ijth emitter, the two rays $\widetilde{\mathbf{p}_{z,ij}}$ and $\widehat{\mathbf{p}_{z,ij}}$ have both the position $\mathbf{h}_{z,ij} = (h_{x,z,ij}, h_{y,z,ij})$, computed using Eqs. (B7) and (B8), and their respective angles are

$$\widetilde{\mathbf{u}_{z,ij}} = \left(\frac{d_{\mathrm{AS}}/2 - h_{x,z,ij}}{z}, \frac{d_{\mathrm{AS}}/2 - h_{y,z,ij}}{z}\right), \tag{B9}$$

$$\widehat{\mathbf{u}_{z,ij}} = \left(\frac{d_{\mathrm{AS}}/2 + h_{x,z,ij}}{z}, \frac{d_{\mathrm{AS}}/2 + h_{y,z,ij}}{z}\right), \tag{B10}$$

where d_{AS} is the diameter of the receiver telescope AS. Each of these rays has an irradiance equal to

$$E_{\mathrm{AS},ij} = \frac{I_{z,ij}\Omega_z\delta_\zeta}{2}, \tag{B11}$$

where δ_ζ is the depth of the considered scattering volume, $I_{z,ij}$ is the ijth component of the intensity grid $\mathbf{I}_z$, and Ω_z is the solid angle subtended by the receiver telescope, computed as

$$\Omega_z = \left(\frac{d_{\mathrm{AS}}}{2z}\right)^2. \tag{B12}$$

In this case, the cosine law [55] is not applied due to the small angles considered. Then, the rays are propagated to the AS using Eq. (B5):

$$\mathbf{p}_{\mathrm{AS}} = \mathbf{M}_{\mathrm{FS}}(z)\mathbf{p}_z. \tag{B13}$$

Assuming an aberration-free system, the receiver telescope is considered as an ideal lens with equivalent focal length f. Then, its action on the rays can be simulated as

$$\mathbf{q}_{\mathrm{AS}} = \mathbf{M}_{\mathrm{IL}}(f)\mathbf{p}_{\mathrm{AS}}, \tag{B14}$$

where $\mathbf{M}_{\mathrm{IL}}$ is the matrix representing an ideal lens with the focal length f:

$$\mathbf{M}_{\mathrm{IL}}(f) = \begin{bmatrix} 1 & 0 \\ -1/f & 1 \end{bmatrix}. \tag{B15}$$

In the case it is needed to simulate the receiver telescope in more detail (e.g., considering field aberrations) and the number of rays representing each emitter can be increased.

5. **Propagating the backscattered wave to the detector plane**: each of the $2 \times n_x \times n_y$ rays traced in the previous step is propagated to the DP using Eq. (B5):

$$\mathbf{q}_{\mathrm{DP}} = \mathbf{M}_{\mathrm{FS}}(f)\mathbf{q}_{\mathrm{AS}}. \tag{B16}$$

Then, the image center and radius of the ijth emitter, defined as $\mathbf{c}_{ij}$ and ρ_{ij}, respectively, are computed as

$$\mathbf{c}_{ij} = \left(\frac{\widetilde{h_{x,\mathrm{DP}}} + \widehat{h_{x,\mathrm{DP}}}}{2}, \frac{\widetilde{h_{y,\mathrm{DP}}} + \widehat{h_{y,\mathrm{DP}}}}{2}\right), \tag{B17}$$

$$\rho_{ij} = \frac{|\widetilde{h_{y,\mathrm{DP}}}| + |\widehat{h_{y,DP}}|}{2}. \tag{B18}$$

In this case it is considered each emitter to have a uniform irradiance, generating $n_x \times n_y$ circles on the DP. If a more detailed simulation is needed (e.g., assuming the emitter's image does not have a uniform irradiance), more rays shall be used for each emitter.

6. **Computing the overlap function**: for each of the $n_x \times n_y$ circles representing the ijth emitter's image on the DP, the intersection with the circle representing the detector area is computed using the circle–circle intersection equation [5]:

$$\begin{aligned}\cap_{ij} &= \rho_{ij}^2 \cos^{-1}\left(\frac{\Delta_{ij}^2 + \rho_{ij}^2 - \rho_d^2}{2\Delta_{ij}\rho_{ij}}\right)\\ &+ \rho_d^2 \cos^{-1}\left(\frac{\Delta_{ij}^2 + \rho_d^2 - \rho_{ij}^2}{2\Delta_{ij}\rho_d}\right)\\ &- \frac{1}{2}\sqrt{\left(-\Delta_{ij} + \rho_{ij} + \rho_d\right)\left(\Delta_{ij} + \rho_{ij} - \rho_d\right)}\\ &\times \sqrt{\left(\Delta_{ij} - \rho_{ij} + \rho_d\right)\left(\Delta_{ij} + \rho_{ij} + \rho_d\right)}, \end{aligned} \tag{B19}$$

where Δ_{ij} is the distance between the emitter's image center and the detector center, considered at $\mathbf{c}_d = (0\ \text{mm}, 0\ \text{mm})$:

$$\Delta_{ij} = \sqrt{c_{x,ij}^2 + c_{y,ij}^2}. \tag{B20}$$

Finally, for each considered range, the overlap function is computed as

$$G_z = \frac{\sum_{i=1}^{N_x} \sum_{j=1}^{N_y} \frac{\cap_{ij}}{\pi \rho_{ij}^2} E_{\mathrm{AS},ij}}{E_{\mathrm{AS}}}. \tag{B21}$$

APPENDIX C: COMPUTING THE OVERLAP FUNCTION USING FO PROPAGATION

Considering an aberration-free system, a transmitted TEM_{00} beam with a waist radius at the TP equal to w_0, the FO propagation method implementation for the different steps presented in Section 3 is the following:

1. **Modeling the transmitted beam**: the beam is expressed as a perturbation $\mathcal{U}_{\mathrm{TP}}(x, y) = A(x, y)\mathrm{e}^{-\mathrm{i}\Phi(x,y)}$, centered on the beam centroid position $\tilde{\mathbf{h}}_0 = (x = 0\ \text{mm}, y = 0\ \text{mm})$, with an amplitude $A(x, y)$ being a Gaussian profile with waist equal to w_0, and a uniform phase $\Phi(x, y)$.
2. **Propagating the beam in the atmosphere**: the beam is propagated to the SP_z using FO,

$$\mathcal{U}_z = \mathcal{P}_{\mathrm{FO}}\left(\mathcal{U}_{\mathrm{TP}}, z\right), \tag{C1}$$

where $\mathcal{P}_{\mathrm{FO}}$ represents one of the three FO propagation methods explained in Appendix A, depending on the propagation range z.

3. **Computing the volume backscattered intensity**: the incident irradiance on the SP_z is computed as

$$E_z = \left|(\mathcal{U}_z)^2\right|. \tag{C2}$$

Then, the volume backscattered intensity is obtained using Eq. (3).

4. **Propagating the backscattered wave to the receiver aperture stop**: the SP_z is divided into $n_x \times n_y$ emitters. Then, the emitters are propagated to the AS using FO,

$$\mathcal{U}_{\mathrm{AS}} = \mathcal{P}_{\mathrm{FO}}\left(\mathcal{U}_z, z\right). \tag{C3}$$

The irradiance of each emitter at the AS is computed using Eq. (4). In the case of an aberration-free system, the AS is a unitary circular aperture, and the action of the receiver telescope on the beam phase is

$$\Phi_{\mathrm{AS}}(x, y) = \mathrm{e}^{-\mathrm{i}\frac{k}{2f}(x^2+y^2)}\Phi_{\mathrm{AS}}(x, y), \tag{C4}$$

where f is the receiver telescope effective focal length, and $\Phi_{\mathrm{AS}}(x, y)$ has been computed in Eq. (C3).

5. **Propagating the backscattered wave to the detector plane**: in this step, each of the $n_x \times n_y$ perturbations at the AS is propagated to the DP,

$$\mathcal{U}_{\mathrm{DP}} = \mathcal{P}_{\mathrm{F0}}\left(\mathcal{U}_{\mathrm{AS}}, f\right). \tag{C5}$$

The irradiance of each emitter on the DP is computed as

$$E_{\mathrm{DP}} = \left|(\mathcal{U}_{\mathrm{DP}})^2\right|. \tag{C6}$$

6. **Computing the overlap function**: finally, for each of the $n_x \times n_y$ emitters' image on the DP, the intersection $\cap_{ij}$ is computed using Eq. (B20) and, for each considered range, the overlap function is computed using Eq. (B21).

APPENDIX D: COMPARING RT AND FO PROPAGATION METHODS

The three FO propagation regions presented in Appendix A have been verified against the analytical equation describing the propagation of a TEM_{00} beam [43]:

$$w_z = w_0\sqrt{1 + \left(\frac{\lambda z}{\pi w_0{}^2 n}\right)^2}, \tag{D1}$$

where w_0 is the beam waist at its focus. In this example, an ideal TEM_{00} beam with waist $w_0 = 5.0$ mm is propagated in the ranges $z = 1$ mm to 100 km. The percentage of the relative error committed using FO propagation method is computed as

$$\varepsilon_w = 100\% \times \left|1 - \frac{w_z}{w_{\mathrm{FO},z}}\right|, \tag{D2}$$

where w_z is computed using Eq. (D1), and $w_{\mathrm{FO},z}$ is the beam size computed using the FO propagation method described in Eqs. (A1), (A5), and (A7), depending on the propagating distance. The obtained results are shown in Fig. 8. The major error committed using FO propagation is in the AnS region, due to numerical errors generated using non-optimized scaling parameters in the discrete Fourier transform (DFT) computation. However, this region is less interesting for the atmospheric lidar design, as atmospheric lidars start to operate at around hundreds of meters. In Fresnel and Fraunhofer regions, the errors are less than 0.2%, ensuring a good simulation of the

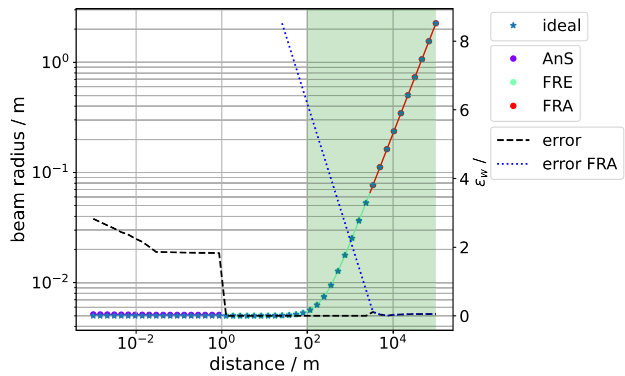

Fig. 8. FO propagation and analytical solution comparison. The analytical TEM_{00} beam propagation solution is represented as blue stars, while the FO propagation results are represented as colored lines. Purple indicates the results obtained in the AnS region; light green, the results for the FRE region; red, the results for the FRA region; black dashed line, the error of the FO propagation with respect to the analytical solution; blue dotted line, the error of the FRA propagation with respect to the analytical solution; and green rectangle represents the usual range of application of lidars, starting at 100 m.

beam propagation. Moreover, the error computed using only the simpler Fraunhofer method is low for almost all the lidars application range, except for very short range lidars, where the error increases, and the Fresnel method should be used.

Funding. Clean Aviation (101101974); European Union.

Acknowledgment. This study was performed within the framework of the UP Wing project. The project Ultra Performance Wing (UP Wing, project number: 101101974) is supported by the Clean Aviation Joint Undertaking and its members. The authors would like to acknowledge Dr. Raoul-Amadeus Lorbeer (Deutsches Zentrum für Luft- und Raumfahrt) for the wise suggestions and for expanding the possible applications of this publication. Moreover, the suggestions of the anonymous reviewers greatly increased the quality of the publication. Many thanks for your time. Co-Funded by the European Union. Views and opinions expressed are however those of the authors only and do not necessarily reflect those of the European Union or Clean Aviation Joint Undertaking. Neither the European Union nor the granting authority can be held responsible for them.

Disclosures. The authors declare no conflicts of interest.

Data availability. Data underlying the results presented in this paper are not publicly available at this time but may be obtained from the authors upon reasonable request.

REFERENCES

1. P. Vrancken and J. Herbst, "Aeronautics application of direct-detection Doppler wind lidar: an adapted design based on a fringe-imaging Michelson interferometer as spectral analyzer," Remote. Sens. **14**, 3356 (2022).
2. C. Geach and B. Kaifler, "Seasonal and altitude dependence of thermospheric metastable helium densities measured by fluorescence lidar," Geophys. Res. Lett. **52**, e2024GL112885 (2025).
3. R. Velotta, B. Bartoli, R. Capobianco, *et al.*, "Analysis of the receiver response in lidar measurements," Appl. Opt. **37**, 6999–7007 (1998).
4. D. Kumar and F. Rocadenbosch, "Determination of the overlap factor and its enhancement for medium-size tropospheric lidar systems: a ray-tracing approach," J. Appl. Remote Sens. **7**, 073591 (2013).
5. T. Halldórsson and J. Langerholc, "Geometrical form factors for the lidar function," Appl. Opt. **17**, 240–244 (1978).
6. K. Stelmaszczyk, M. Dell'Aglio, S. Chudzynski, *et al.*, "Analytical function for lidar geometrical compression form-factor calculations," Appl. Opt. **44**, 1323–1331 (2005).
7. S. W. Dho, Y. J. Park, and H. J. Kong, "Application of geometrical form factor in differential absorption lidar measurement," Opt. Rev. **4**, 521–526 (1997).
8. R. R. Agishev and A. Comeron, "Spatial filtering efficiency of monostatic biaxial lidar: analysis and applications," Appl. Opt. **41**, 7516–7521 (2002).
9. U. Wandinger and A. Ansmann, "Experimental determination of the lidar overlap profile with Raman lidar," Appl. Opt. **41**, 511–514 (2002).
10. J. Su, M. P. McCormick, Z. Liu, *et al.*, "Obtaining a ground-based lidar geometric form factor using coincident spaceborne lidar measurements," Appl. Opt. **49**, 108–113 (2010).
11. J. V. Hey, J. Coupland, M. H. Foo, *et al.*, "Determination of overlap in lidar systems," Appl. Opt. **50** (5791–5797 (2011).
12. A. C. Povey, R. G. Grainger, D. M. Peters, *et al.*, "Estimation of a lidar's overlap function and its calibration by nonlinear regression," Appl. Opt. **51**, 5130–5143 (2012).
13. M. Walker, D. Venable, D. N. Whiteman, *et al.*, "Application of the lamp mapping technique for overlap function for Raman lidar systems," Appl. Opt. **55**, 2551–2558 (2016).
14. A. Comerón, C. Muñoz-Porcar, A. Rodríguez-Gómez, *et al.*, "An explicit formulation for the retrieval of the overlap function in an elastic and Raman aerosol lidar," Atmos. Meas. Tech. **16**, 3015–3025 (2023).
15. I. Berezhnyy, "A combined diffraction and geometrical optics approach for lidar overlap function computation," Opt. Lasers Eng. **47**, 855–859 (2009).
16. P. Kokkalis, G. Georgoussis, A. Papayannis, *et al.*, "Obtaining a ground-based lidar geometric form factor using coincident spaceborne lidar measurements," in *Proceedings of the 8th International Symposium on Tropospheric Profiling* (2009).
17. G. G. Gimmestad and D. W. Roberts, *Lidar Engineering* (Cambridge University Press, 2023).
18. P. Kokkalis, "Using paraxial approximation to describe the optical setup of a typical EARLINET lidar system," Atmos. Meas. Tech. **10**, 3103–3115 (2017).
19. J. Harms, "Lidar return signals for coaxial and noncoaxial systems with central obstruction," Appl. Opt. **18**, 1559–1566 (1979).
20. R. L. Fante, "Electromagnetic Beam Propagation in Turbulent Media," Proc. IEEE **63**, 1669–1692 (1975).
21. L. C. Andrews and R. L. Phillips, *Laser Beam Propagation in Random Media* (SPIE Press, 2005).
22. F. M. Dickey, *Laser Beam Shaping* (Taylor & Francis Group, 2014).
23. T. Shiina, K. Yoshida, M. Ito, *et al.*, "In-line type micropulse lidar with an annular beam: theoretical approach," Appl. Opt. **44**, 7467–7474 (2005).
24. T. Shiina, K. Yoshida, M. Ito, *et al.*, "Long-range propagation of annular beam for lidar application," Opt. Commun. **279**, 159–167 (2007).
25. R. Eixmann, M. Gerding, J. Höffner, *et al.*, "Lidars with narrow FOV for daylight measurements," IEEE Trans. Geosci. Remote. Sens. **53**, 4548–4553 (2015).
26. C. Seckar, L. Guy, A. DiFronzo, *et al.*, "Performance testing of an active boresight mechanism for use in the CALIPSO space bourne LIDAR mission," Proc. SPIE **5877**, 319–330 (2005).
27. L. Fiorani, M. Armenate, R. Capobianco, *et al.*, "Self-aligning lidar for the continuous monitoring of the atmosphere," Appl. Opt. **37**, 4758–4764 (1998).
28. J. Pallotta, P. Ristori, L. Otero, *et al.*, "Remote control and telescope auto-alignment system for multiangle LIDAR under development at CEILAP, Argentina," in *ATMOHEAD Workshop* (2013).
29. M. Di Paolantonio, D. Dionisi, and L. L. Liberti, "A semi-automated procedure for the emitter–receiver geometry characterization of motor-controlled lidars," Atmos. Meas. Tech. **15**, 1217–1231 (2022).
30. G. van Rossum, "Python tutorial," Technical Report CS-R9526 (CWI Report) (1995).
31. G. Giusfredi, *Physical Optics* (Springer, 2019).
32. A. Gerrard and J. M. Burch, *Introduction to Matrix Methods in Optics* (Dover Publications Inc, 1975).
33. G. A. Massey and A. E. Siegman, "Reflection and refraction of Gaussian light beams at tilted ellipsoidal surfaces," Appl. Opt. **8**, 975–978 (1969).
34. J. Arnaud, "Representation of Gaussian beams by complex rays," Appl. Opt. **24**, 538–543 (1985).

35. B. D. Stone and G. W. Forbes, "Characterization of first-order optical properties for asymmetric systems," J. Opt. Soc. Am. **9**, 478–489 (1992).
36. K. S. Yee, "Numerical solution of initial boundary value problems involving Maxwell's equations in isotropic media," IEEE Trans. Antennas Propag. **14**, 302–307 (1966).
37. A. W. Greynolds, "Propagation of generally astigmatic Gaussian beams along skew ray paths," Diffr. Phenom. Opt. Eng. Appl **560**, 33–51 (1986).
38. J. A. Ratcliffe, "Some aspects of diffraction theory and their application to the ionosphere," Rep. Prog. Phys. **19**, 188–267 (1956).
39. J. W. Goodman, *Introduction to Fourier Optics* (McGraw-Hill, 1996).
40. H. Crew, *The Wave Theory of Light: Memoirs of Huygens, Young and Fresnel* (Legare Street Press, 2022).
41. A. Sommerfield, "Mathematische theorie der diffraction," Math. Ann. **47**, 317–374 (1896).
42. R. R. Shannon, *The Art and Science of Optical Design* (Cambridge University Press, 2012).
43. A. E. Siegman, *Lasers* (University Science Books, 1986).
44. R. G. Lane, A. Glindemann, and J. C. Dainty, "Simulation of a Kolmogorov phase screen," Waves Random Media **2**, 209 (1992).
45. J. M. Vaughan, N. J. Geddes, P. H. Flamant, *et al.*, "Establishment of a backscatter coefficient and atmospheric database," ESA-CR12510 22 (1998).
46. V. Pavlou and I. Metaxa, "LIVAS - lidar climatology of vertical aerosol structure for space-based lidar simulation studies," Final Study Report ESTEC Contract No. 4000104106/11/NL/FF/fk, ESA, Penteli, Greece (2013).
47. M. Hess, P. Koepke, and I. Schult, "Optical properties of aerosols and clouds: the software package OPAC," Bull. Am. Meteorol. Soc **79**, 831–844 (1998).
48. G. Mie, "Beiträge zur Optik trüber Medien, speziell kolloidaler metallösungen," Ann. der Physik **330**, 377–445 (1908).
49. S. Prahl, "Miepython: pure python calculation of Mie scattering," Zenodo (2026).https://10.5281/zenodo.7949264
50. C. F. Bohren and D. R. Huffman, *Absorption and Scattering of Light by Small Particles* (Wiley, 1998).
51. J. Gasteiger and M. Wiegner, "MOPSMAP v1.0: a versatile tool for the modeling of aerosol optical properties," Geosci. Model Dev. **11**, 2739–2762 (2018).
52. R. Measures, *Laser Remote Sensing* (John Wiley and Sons, Inc, 1992).
53. D. A. de Wolf, "Electromagnetic reflection from an extended turbulent medium: cumulative forward-scatter single-backscatter approximation," IEEE Trans. Antennas Propag. **19**, 254–262 (1971).
54. A. G. Vinogradov, Y. A. Kravtsov, and V. I. Tatarskii, "The effect of intensification of back scattering by bodies that are situated in a medium having random inhomogeneities," Radiophys Quantum Electron. **16**, 818–823 (1973).
55. W. L. Wolfe, *Introduction to Radiometry* (1998).
56. H. H. Hopkins, *Wave Theory of Aberrations* (Clarendon Press, 1950).
57. M. Born and E. Wolf, *Principles of Optics* (Cambridge University Press, 1999).
58. D. Michel, B. Augère, T. Boulant, *et al.*, "Heterodyne and direct detection wind lidar developed at ONERA," in *LIDAR 2023: 3rd International Workshop on Space-Based Lidar Remote Sensing Techniques Emerging Technologies* (2023).
59. B. Kaifler, C. Geach, H. C. Büdenbender, *et al.*, "Measurements of metastable helium in Earth's atmosphere by resonance lidar," Nat. Commun. **13**, 6042 (2022).
60. R. W. Gerchberg and W. O. Saxton, "A practical algorithm for the determination of phase from image and diffraction plane pictures," Optik **35**, 237–246 (1972).
61. M. Nazarathy and J. Shamir, "Fourier optics described by operator algebra," J. Opt. Soc. Am. **70**, 150–159 (1980).